RSC Advances

PAPER

View Article Online
View Journal | View Issue

Cite this: *RSC Adv.*, 2024, **14**, 17498

ZIF-8/g-C_3N_4 photocatalysts: enhancing CO_2 reduction through improved adsorption and photocatalytic performance†

Yihui Sun,[ab] Hui Zhang,[ab] Yan Lv,[ab] Shengli An[ab] and Ruifen Wang*[ab]

Nowadays, the widespread concern over controlling CO_2 emissions and mitigating the adverse effects of greenhouse gases on global climate has attracted significant attention. In this study, g-C_3N_4 was synthesized by thermopolymerizing urea. Subsequently, ZIF-8 was combined with g-C_3N_4 using an *in situ* deposition method, resulting in the fabrication of ZIF-8/g-C_3N_4 composite photocatalysts at various molar ratios. Effective incorporation of ZIF-8 into g-C_3N_4 suppressed the recombination of photogenerated electrons and holes, thereby enhancing CO_2 capture capacity and preserving light absorption capabilities. The ZIF-8/g-C_3N_4 composite demonstrates excellent photocatalytic performance for CO_2 reduction, where the optimized material exhibited a CO_2 adsorption capacity 1.52 times that of pure g-C_3N_4 and increased the conversion of CO_2 to CH_4 by more than sevenfold. This study harnesses the superior CO_2 adsorption properties of metal–organic frameworks to develop more efficient photocatalysts, enhancing CO_2 conversion efficacy and offering insights for developing efficient photocatalysts that utilize CO_2.

Received 4th April 2024
Accepted 20th May 2024

DOI: 10.1039/d4ra02548b

rsc.li/rsc-advances

1 Introduction

Graphitic carbon nitride (g-C_3N_4) has emerged as a semiconductor material with significant potential in the realm of CO_2 photocatalysis, attributed to its distinctive advantages. This non-metallic semiconductor is composed of carbon and nitrogen, elements abundantly available on Earth. It features a relatively small bandgap of approximately 2.7 eV, enabling a high responsiveness to visible light. Additionally, g-C_3N_4 exhibits superior resistance to acids and bases and maintains its integrity under illumination. Its structure and properties can be readily tailored, offering commendable photocatalytic activity.[1] However, the prevalent issues currently include low photogenerated electron–hole separation efficiency and low CO_2 absorption capacity.[2] Therefore, the development of new materials or the enhancement of CO_2 photocatalytic reduction through doping, compositing to form heterojunctions, and other methods, represents a current research focus. In fact, several adsorbents, such as graphene, activated carbon, zeolites, and certain mesoporous materials, have been employed in conjunction with specific photocatalysts to augment the reduction of CO_2. However, the improvement achieved through these combinations is often quite limited. The catalysts currently in use commonly suffer from issues such as light shielding, photocapture of charges, occupation of redox active sites, and non-selective adsorption of reactants and products.[3]

Metal–organic frameworks (MOFs) are a new class of crystalline porous materials with periodic network structures, self-assembled from metal clusters or metal ions and organic ligands through coordination bonds. They hold significant promise in applications such as adsorption and catalysis. MOF materials have demonstrated strong capabilities in CO_2 adsorption. Based on this, our experiment proposes that combining MOFs with semiconductor photocatalysts can significantly enhance CO_2 capture performance, thereby increasing the efficiency of photocatalytic CO_2 reduction.[4] ZIF-8 (zeolitic imidazolate framework-8) is a type of MOF material with a zeolite topology structure formed by the coordination of Zn^{2+} ions with 2-methylimidazole. ZIF-8 possesses a large specific surface area, high porosity, regular pore channels, good thermal stability, water resistance, CO_2 affinity, and the combined advantages of traditional zeolite molecular sieves and MOFs in terms of chemical stability. Furthermore, it has two other features: one aspect is associated with the inherent transparency of ZIF-8.[5] The integration of ZIF-8 into semiconductor matrices scarcely detracts from their photonic capture capabilities. Another aspect is associated the selective adsorptive properties of ZIF-8. ZIF-8 exhibits a pronounced preference for adsorbing CO_2, the primary reactant, while maintaining a low affinity towards the resultant reduction products, such as CH_4 and CH_3OH.[6]

---

[a] *Key Laboratory of Green Extraction & Efficient Utilization of Light Rare-Earth Resources (Inner Mongolia University of Science and Technology), Ministry of Education, Baotou 014010, China. E-mail: jery19810528@126.com; a979026812@gmail.com*

[b] *College of Rare Earth Industry, Inner Mongolia University of Science and Technology, China*

† Electronic supplementary information (ESI) available. See DOI: https://doi.org/10.1039/d4ra02548b

Moreover, ZIF-8 can typically be synthesized through three common methods: synthesis in methanol solution;[7] synthesis in a mixed solution of methanol and aqueous ammonia;[8] and solvothermal synthesis in DMF.[9] Research has found that ZIF-8(MeOH) has a larger external surface area and more acid–base sites, thus exhibiting significantly higher catalytic activity than ZIF-8(NH_4OH) and ZIF-8 (DMF).[10] Therefore, this study chose to synthesize ZIF-8 by the stirring method and introduced g-C_3N_4 on this basis, modifying ZIF-8 onto the surface of g-C_3N_4 and investigating its enhanced effect on CO_2 reduction performance. The *in situ* prepared ZIF-8/g-C_3N_4 composite material has stronger light capture ability, higher charge separation efficiency, and greater CO_2 absorption capacity. As a result, compared to traditional urea-thermal polymerized g-C_3N_4, the yields of CO and CH_4 are significantly improved, with the yield of CH_4 increasing more than sevenfold.

2 Experimental

2.1 Chemical

All reagents with analytical reagent grade were used as received without further purification. Urea, zinc nitrate hexahydrate, 2-methylimidazole, methanol were purchased from Sinopharm Chemical Reagent Co., Ltd. Deionized water was used throughout the experiment.

2.1.1. The synthesis of g-C_3N_4. g-C_3N_4 was prepared using a high-temperature condensation method, with urea as the precursor. The process involved placing urea in a covered Al_2O_3 crucible, heating from room temperature to 550 °C at a rate of 8 °C min^{-1}, maintaining this temperature for 3 hours, and allowing the material to naturally cool, resulting in the formation of g-C_3N_4.[11]

2.1.2. The synthesis of ZIF-8/g-C_3N_4. Employing an *in situ* method to fabricate ZIF-8/g-C_3N_4 composites. To enhance the integration of ZIF-8 with g-C_3N_4, the experiment first involves the combination of $Zn(NO_3)_2\cdot 6H_2O$ with g-C_3N_4. The specific steps are as follows: 0.63 g of zinc nitrate and 1.26 g of g-C_3N_4 are weighed and added to 60 mL of methanol, followed by ultrasonication for 1 hour, during which the zinc nitrate dissolves. Then, 60 mL of a methanol solution containing 1.6 g of 2-methylimidazole is quickly poured into the above solution, maintained under ultrasonication for 30 minutes, and then mechanically stirred for 8 hours. The mixed solution is centrifuged, and the resultant mixture is dried at 60 °C for 6 hours to obtain the ZIF-8/g-C_3N_4 composite photocatalytic material. To investigate the effects of different ZIF-8 to g-C_3N_4 ratios on the photocatalytic CO_2 reduction performance, experiments were designed with composite photocatalytic materials at different molar percentages of 20%, 40%, 60%, and 80%, denoted as Z20CN, Z40CN, Z60CN, and Z80CN, respectively Pure ZIF-8 was also prepared utilizing the procedure described previously, with the exclusion of g-C_3N_4 addition.

2.2 Characterization of photocatalyst

The phase structure of the catalysts obtained from the experiment was qualitatively analyzed using X-ray diffraction (XRD), with the measurements carried out using a D8-ADVANCE X-ray diffractometer from Bruker, Germany. The micro-morphology of the catalysts was observed using a dual-beam field emission scanning electron microscope (SEM), specifically a GAIA 3 XMN model from TESCAN, Czech Republic, equipped with an energy dispersive X-ray (EDX) scanner for quantitative and qualitative analysis of the elemental distribution within the catalysts. Prior to testing, gold sputtering was performed using a JFC-1600 ion sputter from JEOL Ltd, Japan. High-performance imaging X-ray photoelectron spectroscopy (XPS) was used for qualitative analysis of the composition and chemical states of the catalysts, with measurements taken using an ESCALAB 250Xi from Thermo Fisher Scientific, USA. Binding energies of all samples were calibrated to the C 1s peak at 284.8 eV. FT-IR was employed to analyze the structure and functional groups of the catalysts, using an FT-IR 1200 spectrometer from ST Japan, with pure KBr as the background and a scanning range of 4000 to 500 cm^{-1}. Ultraviolet-visible diffuse reflectance spectroscopy (UV-vis) was used to analyze the light absorption properties of semiconductor materials, their electronic structures, and to calculate the band gap width of semiconductor materials. The measurements were carried out using a U-3900 spectrophotometer from Hitachi, Japan, with a test wavelength range of 200–800 nm. Photoluminescence spectroscopy (PL) was utilized to analyze the migration, transfer, and separation efficiency of photo-generated electron–hole pairs in semiconductors, with the characterization performed using an F-4600 high-performance imaging X-ray photoelectron spectrometer from Hitachi, Japan, obtaining photoluminescence spectra of the samples under an excitation wavelength of 370 nm. Thermogravimetric analysis was conducted in an oxidative atmosphere utilizing a DTG-60H analyzer from Shimadzu, Japan. Nitrogen adsorption–desorption isotherms were quantified using an ASAP2460 from Micromeritics, USA. CO_2 adsorption measurements were performed at room temperature using Micromeritics ASAP 2460 from Micromeritics, USA. Electrochemical testing of the photoelectrochemical properties was performed using a 1260 A + 1287 A electrochemical workstation from Solartron Analytical, UK, with the excitation light source provided by a PLS-SXE300 xenon lamp from Beijing Perfectlight Technology Co., Ltd, and transient photocurrent tests were conducted at 0.1 V for a duration of 540 s.

2.3 Examination of photocatalytic CO_2 reduction performance

In this experiment, a typical gas–solid CO_2 reduction reaction was selected.[12] It is to prevent the impact of water photolysis on the experiment. If a hydrogen source is introduced, the photogenerated charges and energy produced by the catalyst would suffice to meet the demands for both photocatalytic water splitting and CO_2 reduction.[13] The experimental procedure is as follows: the photocatalytic CO_2 reduction performance was evaluated in a 250 mL photoreactor equipped with an optical quartz window. The opening of the reactor was sealed with a silicone stopper, and a 300 W xenon lamp simulating sunlight served as the light source, positioned approximately 15 cm above the reactor. 0.5 mL of H_2O and 50 mg of catalyst powder were added to the sealed glass reactor, uniformly dispersed on a glass plate. Before illumination, the reactor was evacuated and then filled with 20 mL of high-purity CO_2 (99.999%). After 3 hours of light irradiation, the products were analyzed using a gas chromatograph (GC-2014C, Shimadzu, Japan) equipped with a flame ionization detector (FID) and an automatic sampler. The reported gas volumes represent the average of three experimental trials.

3 Results and discussion

3.1 Characterization of the photocatalysts

X-ray diffraction analysis was conducted to study the crystal structure of each sample, with the results shown in (Fig. 1). g-C_3N_4, Z20CN, and Z40CN all exhibited characteristic diffraction peaks of g-C_3N_4 at 12.8° and 27.6° (JCPDS Card No. 87-1526),[14] corresponding to the (100) and (002) planes of g-C_3N_4, respectively.[40] The (100) plane reflects the in-plane periodic arrangement of the tri-*s*-triazine ring structure of the g-C_3N_4 molecular skeleton, while the (002) plane indicates the interlayer stacking of conjugated aromatic ring structures.[15] The strong and pure diffraction peaks of ZIF-8 indicate its high crystallinity. Multiple characteristic crystal planes of ZIF-8, including the (010), (002), (112), and (022) planes, can be observed in the XRD pattern, consistent with previous reports.[16] The standard peaks of the synthesized ZIF-8 were also compared with the simulated ZIF-8 (JCPDS 00-062-1030) and are depicted in Fig. S1.† The diffraction peaks of composites doped with different ratios of ZIF-8 show slight variations. In Z20CN and Z40CN, the (002) plane of g-C_3N_4 is clearly visible, due to the lower doping amount of ZIF-8; however, in Z60CN and Z80CN, the intensity of the (002) peak gradually decreases. Notably, the position of the (002) peak shifts towards a lower angle, indicating an increase in the lattice spacing due to the addition of ZIF-8.[17] As the amount of ZIF-8 increases, the diffraction peaks of ZIF-8 become more prominent while the characteristic peaks of g-C_3N_4 gradually weaken, suggesting an effective composite formation between ZIF-8 and g-C_3N_4.

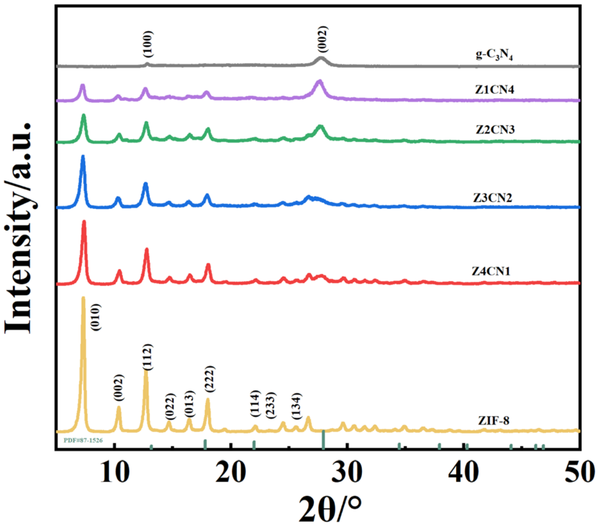

Fig. 1 XRD patterns of diverse photocatalysts.

Field emission scanning electron microscopy (FESEM) and transmission electron microscopy (TEM) were employed to investigate the microstructure of g-C_3N_4, ZIF-8, and Z60CN. As depicted in (Fig. 2a), g-C_3N_4 exhibits a layered stacking of agglomerated clusters,[18] characterized by a relatively loose structure with irregular morphology and size. (Fig. 2b) shows the rhombic dodecahedral morphology of ZIF-8, with microcrystals measuring 80–100 nm in diameter, demonstrating well-crystallized particles, regular shapes, and uniform dispersion.[19] (Fig. 2c) reveals the uniform distribution of ZIF-8 octahedral cubic particles on the surface of g-C_3N_4, with the agglomerated clusters of g-C_3N_4 in the composite product undergoing fragmentation, thereby enhancing the overall particle dispersion and uniformity. The TEM image of Z60CN (Fig. 2d) further confirms the uniform deposition of ZIF-8 on g-C_3N_4 sheets, indicating a tight integration between the two. The energy-dispersive X-ray spectroscopy (EDS) elemental maps of Z60CN (Fig. 2e–h) clearly demonstrate that, beyond the presence of carbon (C) and nitrogen (N), zinc (Zn) is also uniformly distributed within the composite material.[20] These outcomes decisively validate the formation of an effective composite between g-C_3N_4 and ZIF-8, aligning with the X-ray diffraction (XRD) observations detailed earlier.

Thermogravimetric analysis (TGA) under air was utilized to ascertain the actual ZIF-8 loading in the samples. As Fig. 3a illustrates, the three samples demonstrated excellent thermal stability with less than 10% mass loss between 0–350 °C, likely due to the loss of impurities adhered to the surface or within pores, and water adsorbed on the surface. Decomposition of g-C_3N_4 commenced at approximately 550 °C, culminating in complete sublimation and decomposition. ZIF-8 exhibited a weight loss of around 70% from 350 °C to 600 °C, indicative of the metal–organic framework's collapse, leaving ZnO as the residue. Within the same temperature range, Z60CN showed an 85% weight loss, with ZnO being the remaining product, which correlates with ZIF-8 deposited on the Z60CN surface. With ZIF-8 molecular weight at 227.6 g mol^{-1}, including one Zn atom (65.4 g mol^{-1}), the additional ~8% mass loss of Z60CN compared to g-C_3N_4 allowed for the calculation of the actual ZIF-8 loading on the composite Z60CN to be 63.3%. This confirms the actual presence of ZIF-8 in the prepared samples aligns with the designed values.

Fig. 3b delineates the Fourier-transform infrared (FT-IR) spectral profiles for a suite of photocatalysts. The spectral signatures of g-C_3N_4 and ZIF-8/g-C_3N_4 composites exhibit congruent stretching vibrational modes, evidencing that the quintessential lattice structure of g-C_3N_4 is retained after surface modification. The absorption peaks observed in the range of 3000–3500 cm^{-1} for g-C_3N_4 and the ZIF-8/g-C_3N_4 composite samples are attributed to the stretching vibrations of the NH and NH_2 functional groups,[3,21] while the peaks from 1200 to 1630 cm^{-1} are due to the typical stretching vibrations of the g-C_3N_4 heterocycles. The absorption peak at 815 cm^{-1} for both g-C_3N_4 and the composite samples corresponds to the

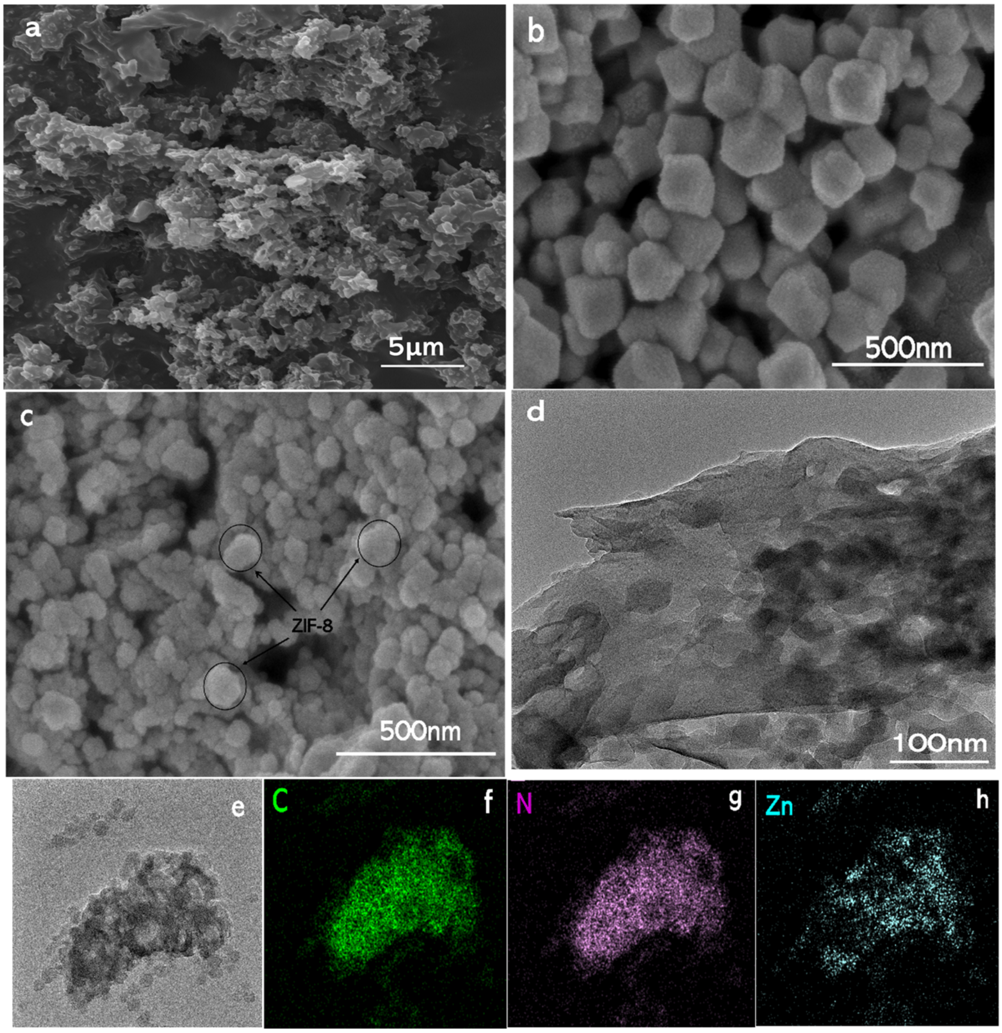

Fig. 2 SEM images of (a) g-C_3N_4 (b) ZIF-8 (c) Z60CN; (d) TEM images of Z60CN; (e–h) the EDX elemental maps of Z60CN.

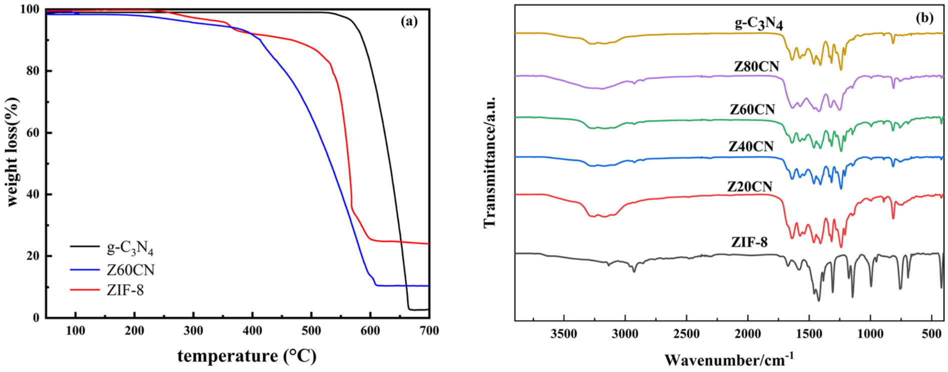

Fig. 3 (a) TG analyses of sample ZIF-8, g-C_3N_4 and Z60CN; (b) the FT-IR spectra of different photocatalysts.

bending vibrations of the triazine structure in g-C_3N_4.[42] The absorption peaks in the range of 1350–900 cm^{-1} and at 800 cm^{-1} are assigned to the in-plane and out-of-plane bending vibrations of the imidazole rings.[22] Notably, the absorption peak at 815 cm^{-1} for the ZIF-8/g-C_3N_4 composite samples shifts to a higher wavenumber, which may originate from structural distortions of the triazine ring units in ZIF-8/g-C_3N_4. Additionally, a new characteristic peak at 422 cm^{-1} appears for ZIF-8 and its composites, corresponding to the stretching vibration of the

Zn–N bond,[23] further corroborating the effective composite formation between the two materials by the *in situ* method.

Fig. 4a–d display the XPS spectra of g-C_3N_4 and Z60CN. As shown in the full scan spectrum in Fig. 4a. C, N, and O elements were detected in both g-C_3N_4 and Z60CN, with the O 1s peak plausibly attributable to the adsorption of CO_2 and H_2O molecules on the sample's surface. The characteristic peak of C 1s at 284.8 eV serves as a charge correction reference for the analysis of the elements. Fig. 4b shows the high-resolution C 1s spectrum, where the characteristic peak in g-C_3N_4 at a binding energy of 287.80 eV corresponds to the sp^2 hybridized orbitals of aromatic N=C–N.[24] In Z60CN, this peak shifts by 0.05 eV to a lower binding energy at 287.75 eV, suggesting effective composite formation between ZIF-8 and g-C_3N_4 and indicating charge transfer or changes in the chemical environment on the surface of the triazine rings. Fig. 4c presents the high-resolution N 1s spectrum, with g-C_3N_4 fitted with two characteristic peaks at 398.45 eV and 400.00 eV, corresponding to the C=N–C within the triazine rings and the bridging nitrogen atoms N–(C)$_3$ hybridized orbitals,[25,26] respectively. The peaks in Z60CN shift to 398.6 eV and 400.2 eV, indicating that the chemical state of N is influenced by the composite of g-C_3N_4 and ZIF-8. Fig. 4d reveals two distinct peaks at 1022.1 eV and 1045.2 eV, corresponding to Zn $2p_{3/2}$ and Zn $2p_{1/2}$, respectively. The observed chemical shifts in the carbon and nitrogen elements in Z60CN relative to g-C_3N_4 further indicate the effective integration of ZIF-8 into the g-C_3N_4 lattice, in alignment with the findings from X-ray diffraction analysis.

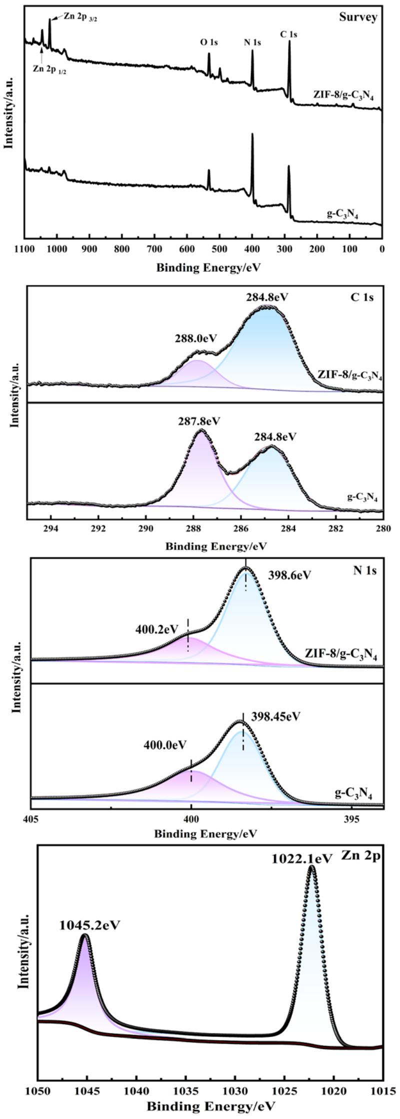

Fig. 4 (a) XPS full scan spectrum of g-C_3N_4 and ZIF-8/g-C_3N_4, (b) C ls, (c) N ls, (d) Zn 2p.

The UV-vis absorption spectra of the samples (Fig. 5a) reveal that the absorption capacity of ZIF-8/g-C_3N_4 in the ultraviolet and visible light regions is enhanced compared to g-C_3N_4, with the absorption edge of each experiencing a red shift. Notably, the absorption edge of Z60CN shifts to 456 nm, indicating a significant improvement in visible light absorption. The bandgap energy (E_g) can be calculated using:

$$\alpha h\nu = A(h\nu - E_g)^{(n/2)}$$

The calculated bandgap energies for g-C_3N_4 and Z60CN are 2.76 eV and 2.71 eV, respectively, indicating that the integration of ZIF-8 reduces the bandgap of g-C_3N_4 by 0.05 eV. Thus, the red shift and the narrowing of the bandgap in Z60CN suggest that it can excite electrons from the valence band to the conduction band at lower energies than g-C_3N_4, potentially enhancing the efficiency of CO_2 reduction during photocatalytic processes.

Fig. 5b presents the photoluminescence (PL) spectra of different photocatalysts. It is observed that the fluorescence intensity of ZIF-8/g-C_3N_4 composites is significantly lower than that of g-C_3N_4, indicating a much slower recombination rate of

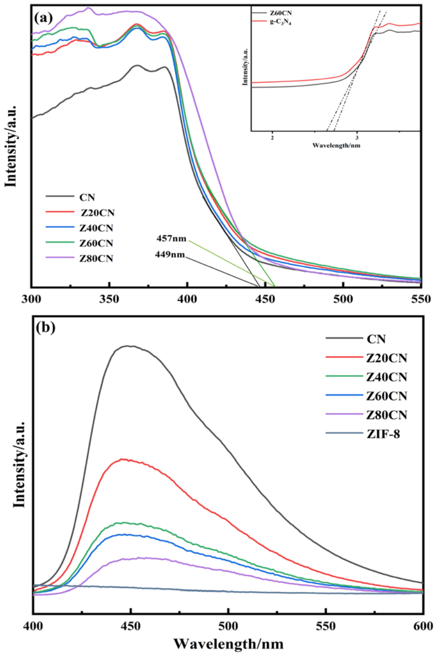

Fig. 5 (a) UV-vis and corresponding relationship between optical energy changes of different samples, (b) PL.

electron–hole pairs in the composites. This slow recombination facilitates more effective separation and migration of electron–hole pairs.[27] Therefore, the introduction of ZIF-8 markedly suppresses the recombination of charge carriers within g-C_3N_4. This suppression contributes to a higher utilization rate of electron–hole pairs,[41] thereby enhancing the activity of the photocatalyst and leading to a more efficient photocatalytic reaction.[28] ZIF-8 not only improves the light absorption properties of g-C_3N_4 but also boosts the photocatalytic efficiency through the diminution of charge carrier recombination rates.

Fig. 6 displays the transient photocurrent response of g-C_3N_4 and Z60CN. The transient photocurrent intensity of Z60CN is notably higher than that of g-C_3N_4, indicating that a greater number of electrons per unit time pass through the Z60CN electrode, which suggests a higher efficiency of photogenerated carrier separation. This is in agreement with the fluorescence test results discussed earlier.

3.2 Adsorption performance

Nitrogen adsorption measurements were employed to characterize the pore structure and specific surface area of the synthesized samples. A larger specific surface area in catalysts typically indicates more adsorption and active sites, which may translate to higher catalytic performance. Fig. 7a presents the adsorption–desorption isotherms of g-C_3N_4 and Z60CN, both of which exhibit type IV classification.[29,30] The presence of H_3 hysteresis loop in the relative pressure (P/P_0) range of 0.60–0.95 suggests the presence of mesopores.[31] The hysteresis loop observed in the isotherms extends across a substantial range of relative pressures, signifying a heterogeneous mesopore size distribution. This is substantiated by the commensurately broad pore-size distributions delineated by the Barrett–Joyner–Halenda (BJH) analysis. Table 1 enumerates the specific surface areas, pore volumes, and average pore diameters for each of the samples. Overall, in this study, the construction of a composite photocatalyst was demonstrated to increase the specific surface area of g-C_3N_4, resulting in more small-sized mesopores.[32]

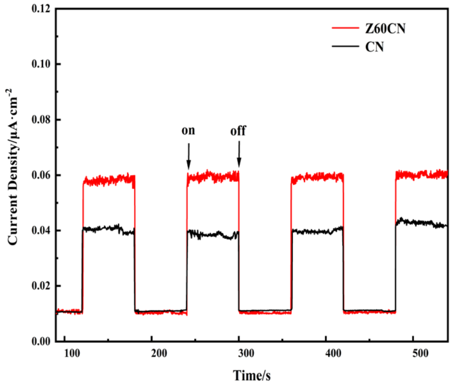

Fig. 6 Transient photocurrent response graphs of g-C_3N_4 and Z60CN.

There is ample literature documenting that the adsorption of CO_2 on the surface of photocatalysts is a primary key step affecting the pathways and kinetics of photocatalytic CO_2 reduction reactions.[33] An in-depth study of the CO_2 adsorption performance of g-C_3N_4, Z60CN, and ZIF-8 samples was conducted *via* CO_2 adsorption isotherms shown in Fig. 7b. Notably, all samples exhibit a linear relationship between CO_2 adsorption capacity and relative pressure (P/P_0) in the range of 0.1 to 1.0.[34] This relationship suggests that the interactions between CO_2 and the samples are predominantly physical.[35] In the relative pressure (P/P_0) range of 0.2–1.0, the CO_2 adsorption capacity of Z60CN is significantly higher than that of pure g-C_3N_4, which is attributable to Z60CN higher specific surface area, thereby exhibiting more pronounced CO_2 adsorption. In summary, the introduction of ZIF-8 to modify the g-C_3N_4 photocatalyst effectively tunes its adsorption properties.[36]

3.3 Photocatalytic CO_2 reduction performance

In a typical gas–solid system, the photocatalytic CO_2 reduction capabilities of all fabricated samples were assessed under irradiation from a 300 watt xenon lamp without an ultraviolet filter. Control experiments confirmed that in the absence of both photocatalyst and light exposure, byproducts such as CO and CH_4 remained undetected. Although it has been demonstrated in recent years that some MOFs exhibit photocatalytic activity

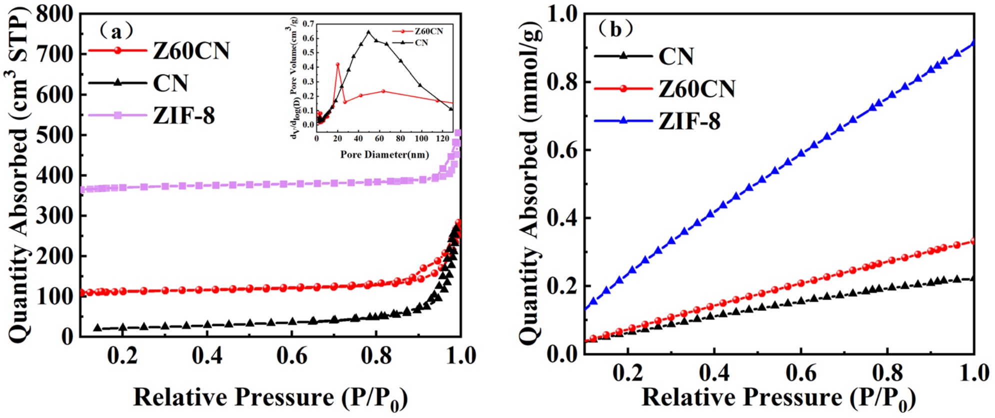

Fig. 7 (a) N_2 adsorption–desorption isotherms and pore size distribution curves of sample CN and Z60CN (b) CO_2 adsorption curves of the sample CN, ZIF-8 and Z60CN.

Table 1 Comparison of the SBET, pore volume, average pore size, CO_2 adsorption

Sample	S_{BET} ($m^2\ g^{-1}$)	Pore volume ($cm^3\ g^{-1}$)	Average pore size (nm)	CO_2 adsorption (mmol g^{-1})
g-C_3N_4	73.87	0.41	22.40	0.21
Z60CN	363.41	0.43	4.80	0.32
ZIF-8	1182.69	0.78	2.64	0.91

for CO_2 reduction under light irradiation,[37] no organic products were detected during prolonged CO_2 photoreduction using pure ZIF-8 as the photocatalyst. This observation that, within the context of this investigation, the presence of both light irradiation and the photocatalyst are essential prerequisites for the effective of CO_2 reduction.

As shown in Fig. 8(a) and (b), as marked increase in the photocatalytic activity for generating CO and CH_4 was achieved with g-C_3N_4 photocatalysts composited with ZIF-8. The total yield of CO and CH_4 increased with the extension of light irradiation time. For Z20CN composited with ZIF-8, the yield of CO production increased by about 70% after 3 hours (Fig. 8a). Meanwhile, for Z60CN composited with ZIF-8, the yield of CH_4 production could be increased by more than 7 times after 3 hours (Fig. 8b). It is important to note that the amount of ZIF-8 composite is crucial for photocatalytic CO_2 reduction. As delineated in earlier discussions, the addition of ZIF-8 substantially amplifies CO_2 capture, serving as an essential preliminary phase to the ensuing photocatalytic conversion of CO_2 into CO and CH_4. It is generally observed that an increase in the CO_2 adsorption capacity of a semiconductor photocatalyst is directly correlated with an improvement in its photocatalytic CO_2 reduction efficacy. Therefore, initially, as the amount of ZIF-8 composite increases, the yield of photocatalytic CH_4 continuously increases. However, the amount of ZIF-8 composite seems to have a dual effect on the performance of photocatalytic CH_4 production. When the molar ratio of ZIF-8 to g-C_3N_4 is 6 : 4 (sample Z60CN), the highest yield of photocatalytic CH_4 production after 3 hours is achieved, reaching 2.56 μmol g^{-1}. Although the introduction of ZIF-8 can enhance CO_2 adsorption, the poor conductivity of ZIF-8 may inhibit surface charge transfer, as also confirmed by the analysis of fluorescence spectra and transient photocurrent responses.[43] To assess the durability of the ZIF-8/g-C_3N_4 composite photocatalyst, we recovered the catalyst after the reactions and conducted XRD comparisons, as shown in Fig. 8(c). The results indicate that the ZIF-8/g-C_3N_4 composite maintains excellent stability for the photocatalytic reduction of CO_2, showing no significant changes in the crystal structure, which suggests its high durability in photocatalytic applications.

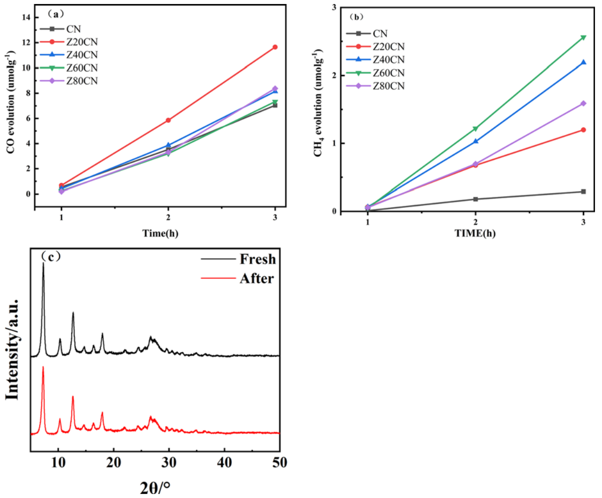

Fig. 8 (a) Comparison of CO production rates for the prepared samples. (b) Comparison of CH_4 production rates for the prepared samples. (c) XRD patterns of Z60CN before and after the catalytic reactions.

In this investigation, across the spectrum of synthesized photocatalysts, CO_2 is predominantly converted into CO and CH_4 as the primary outputs in the photocatalytic reduction process. The possible mechanism for the formation of CH_4 can be described by the following reaction formula,[38] based on the presence of different intermediate products:

$$H_2O + H^+ \rightarrow OH^- + H^+$$

$$2CO^2 + 4e^- + 4h^+ \rightarrow 2CO^2 + O_2$$

$$CO + 6e^- + 6H^+ \rightarrow CH_4 + H_2O$$

Based on the results above, a possible degradation mechanism was proposed in Fig. 9. Although the ZIF-8 in the composite cannot be excited by the visible light, the g-C_3N_4 component can be excited. Under illumination, g-C_3N_4 can be excited to generate electron–hole pairs, with the excited electrons transitioning from the valence band (VB) to the conduction band (CB). The conduction band of ZIF-8 is more negative

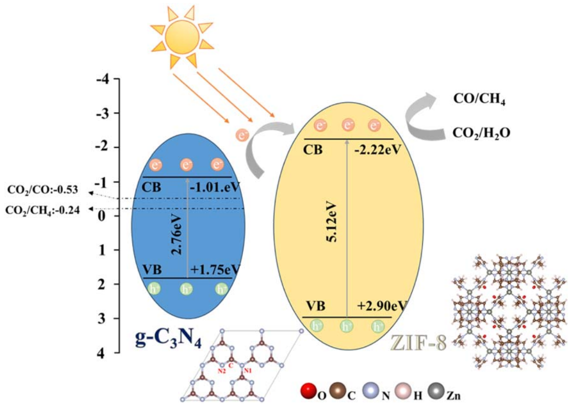

Fig. 9 Mechanism diagram of ZIF-8/g-C_3N_4 photocatalytic CO_2 reduction.

compared to that of g-C_3N_4, prompting the electrons to migrate towards the energetically favorable conduction band of ZIF-8. Given ZIF-8's large surface area and high porosity, it exhibits strong CO_2 adsorption properties. Thus, the electrons flowing to ZIF-8 interact with the adsorbed CO_2. Since the CB potential of ZIF-8 (-2.22 eV) is more negative than the potential of the CO_2/CH_4 redox couple,[39] the accumulated electrons in the CB of ZIF-8 can effectively reduce CO_2 to produce CH_4 and CO.

4 Conclusions

The ZIF-8/g-C_3N_4 series of composite photocatalytic materials was synthesized using an *in situ* deposition method. The designed composite photocatalytic materials largely inherit the optical absorption characteristics of g-C_3N_4, enhance photocatalytic redox capability, improve efficiency of charge separation, and possess excellent CO_2 adsorption capacity. The findings demonstrate that the Z60CN composite photocatalyst displays enhanced photocatalytic performance, reaching a methane production of 2.56 μmol g^{-1} in 3 hours, which is 7 times that of g-C_3N_4, without the addition of a sacrificial agent. Z60CN shows lower photoluminescence (PL) intensity and higher photocurrent density than g-C_3N_4, suggesting that this structure is conducive to interfacial charge transfer. Moreover, ZIF-8's limited inherent conductivity impedes charge transfer within the system. Notably, as the proportion of ZIF-8 in the composite increases, the photocatalytic efficiency of CO_2 reduction for Z80CN declines compared to Z60CN. This illustrates a trade-off between charge transfer efficiency and CO_2 capture capabilities in the composites. Therefore, the precise quantification of ZIF-8 is pivotal in enhancing photocatalytic efficacy. This research offers fresh perspectives on the development of effective CO_2 photocatalysts, leveraging the synergistic interactions between semiconductor nanostructures and metal–organic frameworks.

Author contributions

Y. H. S. and L. Y. synthesized the samples and performed the performance tests. R. F. W and S. L. A. conceived the idea, coordinated all stages of this research, and supervised the work. Y. H. S. and Z. H. wrote the manuscript. All authors contributed to the manuscript.

Conflicts of interest

The authors declare no competing interests.

Acknowledgements

This work was supported by the Inner Mongolia Autonomous Region Science and Technology Program (2021GG0042); Inner Mongolia Autonomous Region Youth Science and Technology Excellence in Higher Education (NJYT22064); Inner Mongolia Autonomous Region Natural Science Foundation Program (2022MS05018) Basic research business cost project in universities (0406082217).

References

1 Y. Zhang, J. Zhou, Q. Feng, *et al.*, Visible light photocatalytic degradation of MB using UiO-66/g-C_3N_4 heterojunction nanocatalyst, *Chemosphere*, 2018, **212**, 523–532.

2 S. Liu, F. Chen, S. Li, *et al.*, Enhanced photocatalytic conversion of greenhouse gas CO_2 into solar fuels over g-C3N4 nanotubes with decorated transparent ZIF-8 nanoclusters, *Appl. Catal., B*, 2017, **211**, 1–10.

3 J. Wen, J. Xie, X. Chen, *et al.*, A review on g-C_3N_4-based photocatalysts, *Appl. Surf. Sci.*, 2017, **391**, 72–123.

4 A. Dhakshinamoorthy, A. M. Asiri and H. Garcia, Metal–organic framework (MOF) compounds: photocatalysts for redox reactions and solar fuel production, *Angew. Chem., Int. Ed.*, 2016, **55**, 5414–5445.

5 S. Liu, J. Wang and J. Yu, ZIF-8 derived bimodal carbon modified ZnO photocatalysts with enhanced photocatalytic CO_2 reduction performance, *RSC Adv.*, 2016, **6**, 59998–60006.

6 Z. Y. Yeo, P. Y. Tan, S. Chai, *et al.*, Continuous polycrystalline ZIF-8 membrane supported on CO_2-selective mixed matrix supports for CO_2/CH_4 separation, *RSC Adv.*, 2014, **4**, 52461–52466.

7 S. R. Venna, J. B. Jasinski and M. A. Carreon, Structural evolution of zeolitic imidazolate framework-8, *J. Am. Chem. Soc.*, 2010, **132**, 18030–18033.

8 C. Chizallet, S. Lazare, D. Bazer-Bachi, *et al.*, Catalysis of transesterification by a nonfunctionalized metal−organic framework: acido–basicity at the external surface of ZIF-8 probed by FTIR and *ab initio* calculations, *J. Am. Chem. Soc.*, 2010, **132**, 12365–12377.

9 U. P. Tran, K. K. Le and N. T. Phan, Expanding applications of metal−organic frameworks: zeolite imidazolate framework ZIF-8 as an efficient heterogeneous catalyst for the knoevenagel reaction, *ACS Catal.*, 2011, **1**, 120–127.

10 Y. Lee, M. Jang, H. Cho, *et al.*, ZIF-8: A comparison of synthesis methods, *Chem. Eng. J.*, 2015, **271**, 276–280.

11 F. Saman, H. Bahruji, A. H. Mahadi, *et al.*, Pd/g-C_3N_4 photocatalyst for hydrogen production: Role of experimental condition for Schottky barrier, *Fuel*, 2023, **349**, 128725.

12 K. M. Kamal, R. Narayan, N. Chandran, *et al.*, Synergistic enhancement of photocatalytic CO_2 reduction by plasmonic Au nanoparticles on TiO_2 decorated N-graphene heterostructure catalyst for high selectivity methane production, *Appl. Catal., B*, 2022, **307**, 121181.

13 W. Dong, J. Jia, Y. Wang, *et al.*, Visible-light-driven solvent-free photocatalytic CO_2 reduction to CO by Co-MOF/Cu_2O heterojunction with superior selectivity, *Chem. Eng. J.*, 2022, **438**, 135622.

14 J. Wang, J. Huang, H. Xie, *et al.*, Synthesis of g-C_3N_4/TiO_2 with enhanced photocatalytic activity for H_2 evolution by a simple method, *Int. J. Hydrogen Energy*, 2014, **39**, 6354–6363.

15 Y. Li, S. Wu, L. Huang, *et al.*, Synthesis of carbon-doped g-C_3N_4 composites with enhanced visible-light photocatalytic activity, *Mater. Lett.*, 2014, **137**, 281–284.

16 N. Hassan, A. Shahat, A. El-Didamony, *et al.*, Equilibrium, Kinetic and Thermodynamic studies of adsorption of cationic dyes from aqueous solution using ZIF-8, *Moroccan J. Chem.*, 2020, **8**, 3–8.

17 X. Guo, S. He, Z. Meng, *et al.*, Ag@ZIF-8/g-C_3N_4 Z-scheme photocatalyst for the enhanced removal of multiple classes of antibiotics by integrated adsorption and photocatalytic degradation under visible light irradiation, *RSC Adv.*, 2022, **12**, 17919–17931.

18 X. Li, B. Wang, W. Yin, *et al.*, Cu^{2+} modified g-C3N4 photocatalysts for visible light photocatalytic properties, *Acta Phys. Chim. Sin.*, 2020, **36**, 1902001.

19 B. Liu, C. Bie, Y. Zhang, *et al.*, Hierarchically porous ZnO/g-C_3N_4 S-scheme heterojunction photocatalyst for efficient H_2O_2 production, *Langmuir*, 2021, **37**, 14114–14124.

20 Y. Zhao, Y. Li, L. Chang, *et al.*, Bimetal doped Cu–Fe-ZIF-8/g-C_3N_4 nanocomposites for the adsorption of tetracycline hydrochloride from water, *RSC Adv.*, 2024, **14**, 4861–4870.

21 M. Tahir, C. Cao, F. K. Butt, *et al.*, Large scale production of novel g-C_3N_4 micro strings with high surface area and versatile photodegradation ability, *CrystEngComm*, 2014, **16**, 1825–1830.

22 Y. Hu, H. Kazemian, S. Rohani, *et al.*, In situ high pressure study of ZIF-8 by FTIR spectroscopy, *Chem. Commun.*, 2011, **47**, 12694–12696.

23 L. Lin, T. Zhang, H. Liu, *et al.*, In situ fabrication of a perfect Pd/ZnO@ZIF-8 core–shell microsphere as an efficient catalyst by a ZnO support-induced ZIF-8 growth strategy, *Nanoscale*, 2015, **7**, 7615–7623.

24 C. Chen, Y. He, G. Xiao, *et al.*, Graphic C_3N_4-assisted dispersion of graphene to improve the corrosion resistance of waterborne epoxy coating, *Prog. Org. Coat.*, 2020, **139**, 105448.

25 H. Cai, D. Han, X. Wang, *et al.*, High specific surface area defective g-C_3N_4 nanosheets with enhanced photocatalytic activity prepared by using glyoxylic acid mediated melamine, *Mater. Chem. Phys.*, 2020, **256**, 123755.

26 C. Saka, Surface modification with oxygen doping of g-C_3N_4 nanoparticles by carbon vacancy for efficient dehydrogenation of sodium borohydride in methanol, *Fuel*, 2022, **310**, 122444.

27 L. Jiang, X. Yuan, Y. Pan, *et al.*, Doping of graphitic carbon nitride for photocatalysis: a review, *Appl. Catal., B*, 2017, **217**, 388–406.

28 X. Liu, J. Zhang, Y. Dong, *et al.*, A facile approach for the synthesis of Z-scheme photocatalyst ZIF-8/g-C_3N_4 with highly enhanced photocatalytic activity under simulated sunlight, *New J. Chem.*, 2018, **42**, 12180–12187.

29 K. S. Sing, Reporting physisorption data for gas/solid systems with special reference to the determination of surface area and porosity (Recommendations 1984), *Pure Appl. Chem.*, 1985, **57**, 603–619.

30 L. Wang, P. Jin, S. Duan, *et al.*, In-situ incorporation of Copper (II) porphyrin functionalized zirconium MOF and TiO_2 for efficient photocatalytic CO_2 reduction, *Sci. Bull.*, 2019, **64**, 926–933.

31 G. Tzvetkov, M. Tsvetkov and T. Spassov, Ammonia-evaporation-induced construction of three-dimensional NiO/g-C_3N_4 composite with enhanced adsorption and visible light-driven photocatalytic performance, *Superlattices Microstruct.*, 2018, **119**, 122–133.

32 Y. Zhou, L. Zhang, W. Huang, *et al.*, N-doped graphitic carbon-incorporated g-C_3N_4 for remarkably enhanced photocatalytic H2 evolution under visible light, *Carbon*, 2016, **99**, 111–117.

33 Q. Huang, J. Yu, S. Cao, *et al.*, Efficient photocatalytic reduction of CO_2 by amine-functionalized g-C_3N_4, *Appl. Surf. Sci.*, 2015, **358**, 350–355.

34 J. Yu, S. Wang, B. Cheng, *et al.*, Noble metal-free Ni $(OH)_2$-g-C_3N_4 composite photocatalyst with enhanced visible-light photocatalytic H_2-production activity, *Catal. Sci. Technol.*, 2013, **3**, 1782–1789.

35 Z. Sun, Z. Yang, H. Liu, *et al.*, Visible-light CO_2 photocatalytic reduction performance of ball-flower-like Bi_2WO_6 synthesized without organic precursor: effect of post-calcination and water vapor, *Appl. Surf. Sci.*, 2014, **315**, 360–367.

36 K. K. Han, C. C. Wang, Y. Y. Li, *et al.*, Facile template-free synthesis of porous g-C_3N_4 with high photocatalytic performance under visible light, *RSC Adv.*, 2013, **3**, 9465–9469.

37 D. Li, M. Kassymova, X. Cai, *et al.*, Photocatalytic CO_2 reduction over metal-organic framework-based materials, *Coord. Chem. Rev.*, 2020, **412**, 213262.

38 O. K. Varghese, M. Paulose, T. J. LaTempa, *et al.*, High-rate solar photocatalytic conversion of CO_2 and water vapor to hydrocarbon fuels, *Nano Lett.*, 2009, **9**, 731–737.

39 C. Chen, J. Jin, S. Chen, *et al.*, *In situ* growth of ultrafine ZnO on g-C_3N_4 layer for highly active and selective CO_2 photoreduction to CH4 under visible light, *Mater. Res. Bull.*, 2021, **137**, 111177.

40 H. He, Z. Luo and C. Yu, Diatomite-anchored g-C_3N_4 nanosheets for selective removal of organic dyes, *J. Alloys Compd.*, 2020, **816**, 152652.

41 Y. Yang, J. Wu, B. Cheng, *et al.*, Enhanced photocatalytic H_2-production activity of CdS nanoflower using single atom Pt and graphene quantum dot as dual cocatalysts, *Chin. J. Struct. Chem.*, 2022, **41**, 2206006–2206014.

42 C. Yu, H. He, W. Zhou, *et al.*, Novel rugby-ball-like $Zn_3(PO_4)_2$@C_3N_4 photocatalyst with highly enhanced visible-light photocatalytic performance, *Sep. Purif. Technol.*, 2019, **217**, 137–146.

43 F. Hong-Ru, Y. Jiang, L. Jia-Hua, *et al.*, A robust heterometallic Cd(II)/Ba(II)-organic framework with exposed amino group and active sites exhibiting excellent CO_2/CH_4 and C_2H_2/CH_4 separation, *Chin. J. Struct. Chem.*, 2022, **41**, 2203287–2203292.